geomatics

MDPI

Article

Impact of UAV Photogrammetric Flight and Processing Parameters on Terrain Modelling Accuracy in Ageing Deciduous and Mixed Forests: A SHAP-Based Analysis

Botond Szász *, Gábor Brolly and Géza Király

Institute of Geomatics and Civil Engineering, Faculty of Forestry, University of Sopron, 9400 Sopron, Hungary; brolly.gabor@uni-sopron.hu (G.B.); kiraly.geza@uni-sopron.hu (G.K.)
* Correspondence: szasz.botond@uni-sopron.hu

Abstract

In this study, we investigated the effects of flight and processing parameters on the accuracy of UAV-based photogrammetric digital terrain models (DTM) generated from RGB imagery in ageing deciduous and mixed forest stands. Four 100 × 100 m sample plots were selected, for which the reference terrain surface was established using terrestrial laser scanning. Photogrammetric DTMs derived from various parameter combinations were compared against this reference, analysing the magnitude of deviations and the influence of individual parameters through SHAP (SHapley Additive exPlanations) analysis. Based on the identified effects, we provide recommendations for optimal workflows and parameter settings. The processing chain also incorporates a targeted raster-level smoothing procedure developed by the authors, which effectively removes DTM errors caused by point cloud noise left by filtering algorithms, thereby reducing extreme deviations from the reference surface. The results show that the absolute mean elevation error is primarily influenced by flight parameters and ground point classification scale (parameter of the lasground algorithm). Optimal flight parameters were determined at a flight altitude of 100 m, with 80% front and 90% side overlap. Furthermore, a ground classification scale of 9 m proved optimal in forested environments. The proposed targeted smoothing significantly reduced extreme errors, yielding DTMs with a mean error of approximately 6 cm and maximum deviations of about 40 cm. These accuracies demonstrate that UAV-based photogrammetry, when carefully parameterised, provides a reliable basis for surface model normalization and subsequent forest structural analyses.

Keywords: UAV photogrammetry; digital terrain model; ground classification; point cloud filtering; SHAP analysis; parameter sensitivity

Academic Editor: Antonio Vettore

Received: 30 December 2025
Revised: 3 February 2026
Accepted: 7 February 2026
Published: 11 February 2026

1. Introduction

Over the past decade, the rapid development of unmanned aerial vehicles (UAVs) and various optical sensors has fundamentally transformed the methodology of forestry remote sensing. UAV-based photogrammetry is now capable of providing spatial data in a fast and cost-effective manner.

The production of a digital terrain model (DTM), which is essential for an accurate and reliable representation of the ground surface, is one of the key requirements of forestry applications of remote sensing. Tree height determination [1–3], volume estimation [4], as well as biomass modelling [5–7], carbon stock estimation [8,9], and yield analysis [10] are

all fundamental tasks that are highly sensitive to the accuracy of terrain models. At the same time, the closed forest canopy, terrain variability, and vegetation heterogeneity pose significant challenges to the high-resolution reconstruction of the ground surface.

Although photogrammetric processing is widely applied, a detailed and quantitative investigation of the effects of different combinations of flight and processing parameters remains limited in forestry practice, with only a few examples available in the literature. One such example is the study by Pessacg et al. [11], who analysed the impacts of various flight and ODM-based (OpenDroneMap) processing parameters. A precise understanding of the influence of input variables not only supports methodological optimisation but also contributes to reducing model uncertainty and improving the reliability of forestry indicators derived from remote sensing data. Accordingly, it is essential to apply analytical frameworks that can reveal both the direct and interaction effects of parameters on the accuracy of the resulting DTMs.

1.1. UAV-Based Photogrammetry

UAV-based aerial photogrammetry essentially consists of six steps: flight planning, placement of ground control points, image acquisition, image matching, point cloud and model generation, and data analysis [12]. The geometric resolution and accuracy of the acquired images—and consequently of the derived models—are influenced by flight parameters. Camera specifications (sensor size, pixel size, focal length) determine the ground area represented by a single pixel as a function of flight altitude. Image overlap primarily affects flight duration and the image matching process. According to Dhruva et al. [13], from a forestry perspective, a flight altitude of 120 m combined with 90% front overlap and 85% side overlap is optimal; although reducing the altitude to 80 m improves geometric resolution, the resulting models tend to be more prone to errors. Although their study did not focus on forested environments, Nikolakopoulos et al. [14] suggest flight altitudes between 70 and 110 m, corresponding to a ground sampling distance of approximately 3 cm/pixel, for steep terrains to achieve centimetre-level accuracy.

For mapping purposes, nadir (i.e., vertically downward-looking) images are typically acquired. Kyriou et al. [15] identified a relationship between terrain characteristics and image acquisition geometry. Sadeq [16] demonstrated that the inclusion of oblique images alongside nadir imagery leads to more reliable photogrammetric products. Similar conclusions were drawn by Ahmed et al. [17], who combined nadir images with images captured at a 70° tilt angle. They further noted that a significant increase in reliability was achieved when the flight lines used for capturing oblique images were oriented perpendicular to the flight path used for nadir image acquisition. This improvement in reliability is especially pronounced in areas with built structures and vertical surfaces [18,19], and in complex terrain characterized by slopes steeper than 60°.

1.2. Ground Control Points and Image Matching

The purpose of ground control points (GCPs) is to improve the accuracy of the derived products and to ensure their precise alignment within a defined coordinate reference system. The necessity of their use is determined by the accuracy requirements imposed on the models. If the mean vertical error of a model is required to be below 12 cm, according to Hugenholtz et al. [20], direct georeferencing based solely on camera positions is insufficient, and the use of GCPs becomes necessary. However, the results of Štroner et al. [21] indicate that even without the use of GCPs, relying solely on the UAV's RTK positioning, an average vertical error below 10 cm can be achieved, when the study area exhibits sufficient variability and is thus well suited for SfM-based processing (see below).

The number of ground control points fundamentally influences the accuracy of the generated three-dimensional models. Tahar [22] investigated six different GCP configurations (ranging from 4 to 9 points) over an area of 1.5 km^2 and found that although the accuracy was satisfying in all cases, the results obtained using 8 and 9 GCPs clearly outperformed the other configurations. According to Sanz-Ablanedo et al. [23], when fewer GCPs are used, the three-dimensional root mean square error (RMSE) of the resulting model is expected to be approximately ±five times the geometric resolution of the model. However, when at least two GCPs are placed per each block of 100 images, this error can be reduced to approximately twice the geometric resolution.

Image matching is an automatic process aimed at identifying identical points, features, or structures between overlapping images [24]. Over recent years, numerous image-matching methods and algorithms have been developed, including SIFT (Scale-Invariant Feature Transform), SURF (Speeded-Up Robust Features), ORB (Oriented FAST and Rotated BRIEF) [25], SGM (Semi-Global Matching) [26], MVS (Multi-View Stereo) [27], and SfM (Structure-from-Motion) [28].

Among these approaches, the SfM algorithm has become one of the most widely adopted across various disciplines, including forestry applications, due to its simplicity and relatively low operational cost [29]. The method simultaneously estimates the internal and external orientation parameters while generating a sparse point cloud based on tie points. Its most significant advantage is that it does not require a pre-calibrated camera, allowing images acquired with non-professional imaging systems to be processed reliably [30]. Harwin et al. [31] demonstrated that SfM-based camera calibration outperformed traditional approaches even in cases where prior calibration data were available, particularly when nadir images were complemented with oblique camera orientations.

1.3. Noise Filtering and Ground Point Classification

Surface models—including terrain models—are derived from point clouds originating from various data sources, where each point is described by three-dimensional XYZ coordinates. According to Polat and Uysal [32], both airborne LiDAR-based and photogrammetric point clouds are suitable for generating models with adequate accuracy; however, they emphasize that photogrammetric results are particularly sensitive to camera characteristics, flight altitude, applied software solutions, and illumination conditions.

Noise filtering is a crucial step, especially for photogrammetric point clouds, as texture-poor or repetitive surfaces degrade tie-point detection. This issue is further exacerbated by inconsistencies between images captured under different seasonal and illumination conditions, while minor errors in camera calibration and positioning can be significantly amplified in the final reconstruction [33]. Various approaches have been proposed for point cloud noise filtering. Ren et al. [34] applied statistical filtering to remove large-scale noise occurring on relatively smooth surfaces, while bilateral filtering was used near breaklines to preserve small-scale features and prevent the blurring of important edges. Wang et al. [35] incorporated reliability measures associated with individual points, whereas Salehi et al. [36] employed a RANSAC-based filtering approach.

The generation of DTMs is a complex process, as these models are intended to represent the ground surface exclusively, with all above-ground objects removed. Consequently, the initial step involves the identification and classification of ground points within the point cloud. Ground point classification is one of the most critical stages of terrain modelling. Liu [37] proposed point cloud thinning as an initial processing step, during which data density is reduced while ensuring the preservation of key topographic features—such as breaklines, ditches, and ridges—while less relevant points are removed. A reliable and detailed terrain model can then be generated from the classified ground points.

All ground point classification methods rely on assumptions regarding the spatial distribution of ground points within a local neighbourhood, which are expected to conform to a parametrically defined surface [38]. Based on this principle, four main conceptual approaches can be distinguished: slope-based [39,40], block-minimum [41,42], surface-based [43,44], and clustering/segmentation-based methods [45,46]. The review by Meng et al. [47] provides a comprehensive overview of ground point classification algorithms, while Klápště et al. [48] specifically investigated the sensitivity of procedures implemented in commonly used software packages.

Kraus and Pfeifer [49] introduced a strip-based ground point classification method, from which a terrain model was subsequently generated through averaging. Shortly thereafter, the first adaptive triangulated irregular network (TIN) fitting approaches were developed [50]. These methods, known as Progressive TIN Densification (PTD) algorithms, gradually increase the density of the terrain points though the iterative refinement of a TIN model that approximates the ground surface. Dong et al. [51] reduced the ratio of misclassified terrain points (Type I error) by proposing an improved method that divides the filtering process into two stages. The first stage follows the standard PTD iterative densification approach, which transitions to the second stage once the density of TIN-associated points exceeds a predefined threshold. In this second stage, a multiscale iterative densification strategy is introduced, resulting in a larger angular threshold and consequently reducing Type I errors and total errors by 7.53% and 4.09%, respectively.

Morphological filters are also well suited for ground point classification. The Simple Morphological Filter (SMRF) applies a linearly increasing window size and a simple slope threshold, serving as a stable baseline from which more advanced progressive filters can be developed. This approach is particularly effective in minimising Type I error rates while maintaining acceptable Type II error rates, thereby preserving fine-scale surface features [52]. Zhang et al. [53] introduced a progressive filter capable of removing smaller objects (e.g., trees) relative to larger structures (e.g., buildings) simultaneously. Although terrain underestimation typically occurs beneath the removed surface regions, the method resulted in only a 3% error at control points.

As an alternative approach, Zhang et al. [54] proposed the Cloth Simulation Filter (CSF), in which the point cloud is first inverted and then covered with a rigid cloth surface. By analysing the interactions between cloth nodes and point cloud points, an approximation of the ground surface is simulated, enabling ground point classification. The resulting surface model exhibited a 4.58% error relative to the reference terrain. Li et al. [55] further enhanced this method by incorporating an additional parameter representing local terrain variability, thereby increasing the adaptivity of the approach. Cai et al. [56] presented and further developed a combined application of CSF and PTD algorithms, achieving results that outperformed those of both individual methods.

2. Materials and Methods

2.1. Selection of Sample Areas and Collection of Reference Data

For the accuracy assessment, we selected sample areas that are located in ageing forest stands, exhibit mixed species composition (deciduous and coniferous species), contain only minimal shrub layers, and are characterised by heterogeneous terrain conditions. The sample areas were defined with an extent of 100 × 100 m, and a total of four areas were selected (Figure 1). The main forestry characteristics of the forest subcompartments containing the sample plots are summarized by tree species in Table 1. The forest subcompartment including Sample area 3 exhibits lower canopy closure and stem density due to the initiation of a gradual regeneration cutting; however, the designated sample plot itself does not directly overlap with the treated stand section.

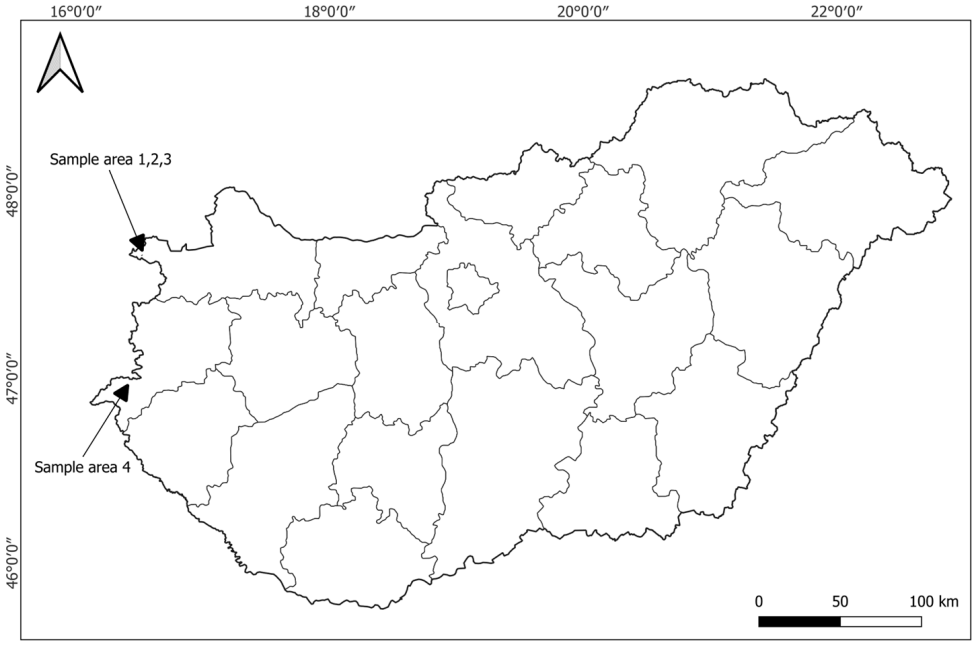

Figure 1. Position of sample areas in Hungary.

Table 1. Main forestry characteristics of the forest subcompartments containing the sample areas.

Sample Area	Forest Type	Age [Years]	Canopy Closure [%]	Species	Species Proportion [%]	Stem Density [ha^{-1}]	Diameter at Breast Height [cm]	Mean Tree Height [m]
1	mixed deciduous–sessile oak forest	64	77	Sessile oak	49	277	25	20
				Beech	35	216	25	22
				Hornbeam	5	39	18	18
				Red oak	9	39	28	21
				Norway spruce	2	10	25	22
2	sessile oak–Scots pine forest	95	75	Sessile oak	29	138	28	22
				Scots pine	51	269	28	23
				Beech	12	47	33	24
				Hornbeam	5	26	22	18
				Norway spruce	3	22	27	25
3	sessile oak–beech forest	119	54	Beech	52	99	45	29
				Sessile oak	19	38	41	26
				Larch	16	58	37	29
				Norway spruce	8	31	36	31
				Scots pine	2	8	34	25
				Black pine	3	9	38	25
4	Scots pine–sessile oak forest	85	73	Sessile oak	51	166	34	24
				Beech	13	44	35	26
				Scots pine	25	101	31	24
				Hornbeam	7	32	22	18
				Norway spruce	4	25	29	27

The point clouds required for generating the reference DTMs were acquired using terrestrial laser scanning (TLS), as these data were also intended for subsequent forest stand structural analyses. Scanning was performed using a Leica ScanStation P40 (Leica Geosystems, Heerbrugg, Switzerland), which can acquire points at distances of up to 270 m, with a maximum acquisition rate of 1 million points per second and an accuracy of 0.5 mm at a range of 50 m. The registration of the point cloud was carried out in the Leica Cyclone (v2025.0.0) software environment using a target-based registration approach based on geodetic control points, since the reference targets used for the registration were previously surveyed and permanently stabilized. Consequently, the accuracy of the registration is primarily governed by the accuracy of the geodetic control points and the applied positioning methods.

The coordinates of the scan positions were determined depending on site-specific conditions (satellite visibility, availability and strength of mobile network coverage, and visibility from established control points) using real-time kinematic (RTK) and post-processed static (PP) GNSS positioning, geodetic traversing, polar measurements, and free-station setups. A Leica GS16 GNSS receiver was used for satellite-based positioning, while a Leica TS03 total station, with an angular accuracy of 2″ and a distance accuracy of 1 mm + 1.5 ppm, was employed for traversing, polar measurements, and free-station observations in conjunction with the laser scanner. Post-processing of the static GNSS measurements was performed using Leica GeoOffice (v8.4) software. The average RMS value of the satellite-based determination of point coordinates was approximately 3 cm.

The number and spatial distribution of scan positions were influenced by forest stand density and terrain characteristics. The positions are illustrated in Figure 2, where contour lines are demonstrating their placement.

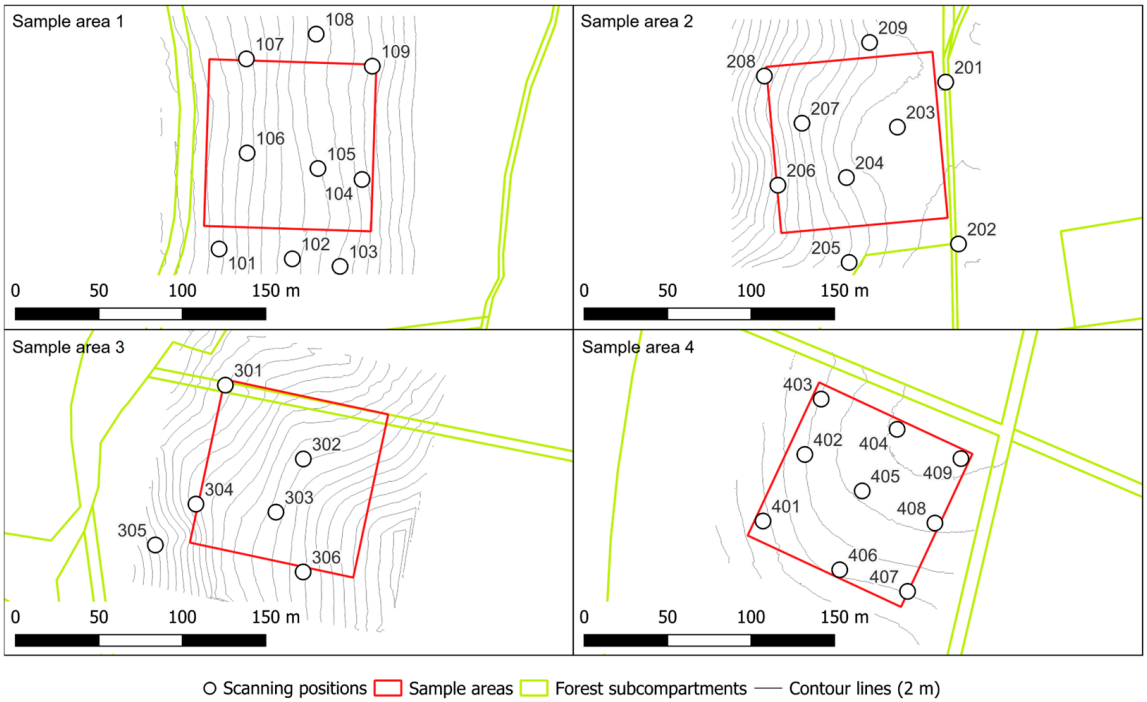

Figure 2. TLS scanning positions (with unique identifiers) overlaid on contour maps to illustrate local terrain characteristics.

2.2. Flight Planning, Execution, and Placement of Ground Control Points

A DJI Mavic 2 Pro UAV (SZ DJI Technology Ltd., Shenzhen, China) was used for aerial image acquisition, while flight planning was carried out using the cloud-based DroneDeploy software (https://www.dronedeploy.com/) (DroneDeploy Inc., San Francisco, CA, USA).

Flights were planned at three different altitudes (80, 100, and 120 m), using a single-grid flight pattern with 90% front overlap and 90% side overlap. The orientation of the flight lines was influenced by the spatial distribution of clearings and corridors suitable for ground control point placement. All images were acquired in nadir orientation, and no oblique images were captured, as the terrain did not include extreme geomorphological features. Image acquisition was performed using a distance-based interval, the spacing of which was determined by ground sampling distance and front overlap. Based on these parameters and the time required by the UAV to capture successive images (2 s in this case), the flight planning software calculated the flight speed, which was set to 3 m/s at flight altitudes of 80 and 100 m, and to 4 m/s at 120 m.

When defining the flight area, the primary consideration was to ensure that every point within each sample area was captured from as many viewing angles as possible, thereby avoiding reduced reliability toward the boundaries of the sample areas due to fewer image perspectives. As a result, the boundaries of the flight areas extend well beyond the actual limits of the sample areas (Figure 3). The flight planning software allows for terrain-following flights using an SRTM-based digital elevation model [57], thereby mitigating variations in overlap caused by changing topographic conditions.

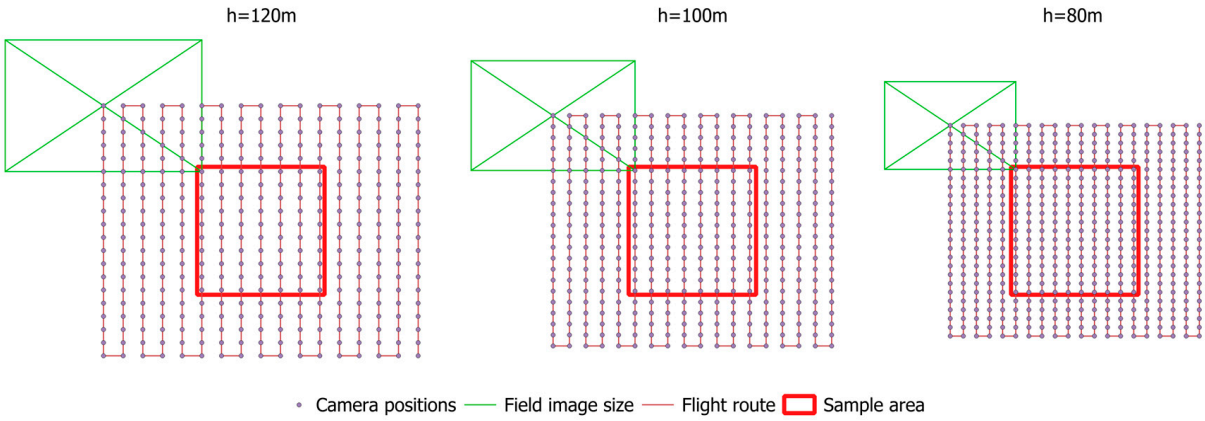

Figure 3. Flight route and field image size at the tree different flight altitudes.

To ensure accurate image orientation, ground control points (GCPs) were placed and measured in the field. Their placement was determined by visibility requirements; consequently, they were positioned in forest openings and canopy gaps. Ideally, the GCPs cover the entire extent of the sample areas; however, in some cases, this was not fully achievable due to the lack of suitably located openings and gaps in proximity (Figure 4).

The applied GCPs consisted of square, 30 × 30 cm cross-coded targets, divided into four quadrants with alternating black and white coloration. This high-contrast pattern ensures reliable and unambiguous identification of the target centre in the aerial imagery and improves the precision of image orientation. An example of the applied ground control point is shown in Figure 5.

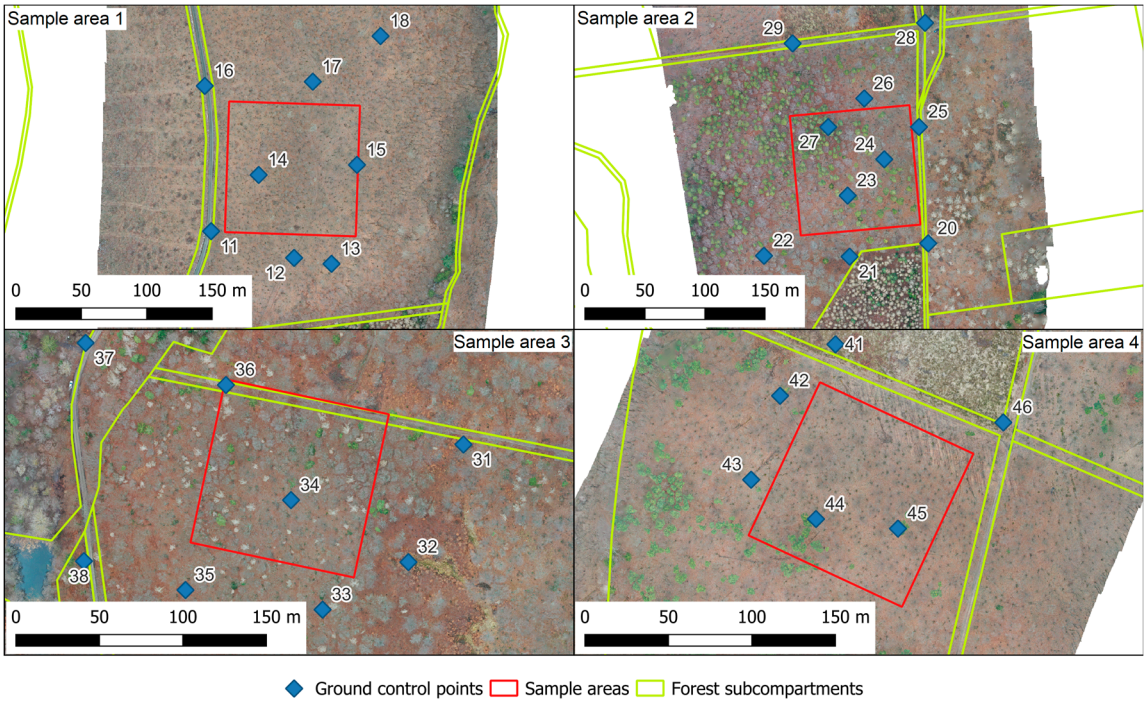

Figure 4. Spatial distribution of ground control points (with unique identifiers) and sample areas overlaid on the orthomosaics.

Figure 5. Example of a ground control point used in the survey.

2.3. Point Cloud Generation, Filtering, and Model Construction

Photogrammetric processing of the acquired aerial images was performed using Agisoft Metashape v2.0.2 (Agisoft LLC, St. Petersburg, Russia). Although image overlap was set to 90% in both directions during flight planning, overlaps of 80% and 70% were simulated through image filtering. Considering the three flight altitudes and the different front and side overlap values, a total of 27 parameter combinations were possible for each sample area. Image alignment was performed using the high accuracy setting, with a key point limit of 50,000 and a tie point limit of 10,000, applying both generic and reference preselection. However, as lower overlap values may result in insufficient image matching quality, the subsequent processing steps were applied only in cases where at least 90% of the images were successfully oriented. Where this criterion was not met, image alignment was repeated without using the preselection options.

Dense point cloud generation was also performed using the high-quality setting, meaning that every second pixel of each image was taken into account. Although the highest setting, which utilises every pixel, produces denser point clouds, it also significantly increases point cloud noise [58].

In addition to spatial coordinates and colour information, the generated points are associated with a confidence metric, which serves as a relative indicator of reconstruction reliability. To assess the influence of low-reliability points on the final models, the workflow was split into two branches: one branch retained the raw point cloud, while the other removed points with a confidence value of 1, resulting in a reduced point cloud.

Although Metashape is capable of further point cloud processing, ground point classification, and generation of 3D and elevation models, these steps were carried out using LAStools (rapidlasso GmbH, Gliching, Germany) software due to its significantly superior and more flexible parameterisation options. Although originally developed for processing LiDAR-derived point clouds, LAStools is also capable of handling photogrammetric point clouds. The processing workflow utilised the lasthin, lasnoise, lasground, and las2dem modules with various parameter settings and combinations.

The lasthin module thins the point cloud based on a regular grid of a specified cell size, retaining a single point per cell. A parameter allows for the selection of which point to retain based on vertical ordering (e.g., the nth lowest or highest point). In this study, five branches were created by retaining the first, second, third, fourth, and fifth lowest points within each 5 × 5 cm cell.

The lasnoise algorithm was then applied to the thinned point clouds. As its name suggests, this module performs noise filtering by removing isolated points or small point clusters located beyond a specified distance from larger point groups. At this stage, the workflow again branched into two paths: application of the noise filter (with a 10 cm threshold) or omission of this step.

Further branching occurred during ground point classification using the lasground module, which classifies ground points based on a user-defined scale parameter. Smaller scale values preserve finer details. In this study, ten different scale values ranging from 3 to 12 m were tested.

Prior to DTM generation, an additional custom-developed step was applied: filtering ground points based on height variation within a regular grid of a specified cell size. The algorithm evaluates the standard deviation of point elevations within each cell; if it exceeds a predefined threshold, all points within that cell are removed, and the cell height is later interpolated from surrounding values during rasterization. This step is necessary because ground point classification may incorrectly retain points representing boulders, stumps, or tree trunks. Residual noise below the ground surface can also be eliminated using this approach. Accordingly, this stage also split into two branches: application of the filter using 25 × 25 cm cells, or omission of the filter.

The point clouds processed through the various parameter combinations were rasterised using the las2dem module. The resulting terrain models had a spatial resolution of 0.25 m per pixel.

The final processing step, developed by us, was applied to the created models. This step consists of a targeted smoothing algorithm designed to remove remaining small protrusions (e.g., stumps or artificial pits caused by sub-ground noise). The algorithm analyses all possible one-dimensional chains (vectors) of pixel elevation values:

$$v = \{z_1, z_2, \ldots, z_n\}, \tag{1}$$

with a specified odd length n across the entire model, in both north–south and east–west directions, where the central pixel index is given by:

$$c = \frac{n+1}{2}. \tag{2}$$

Within these vectors, pits, half-pits, peaks, and half-peaks are detected.

For pits and peaks, the analysis starts from the central pixel (c) of the vector and proceeds outward in both directions, evaluating elevation differences between adjacent pixels. The slope percentage between two neighbouring pixels is defined as follows:

$$s_k = \frac{z_{k+1} - z_k}{r}, \tag{3}$$

where r denotes the spatial resolution of the raster. If the absolute slope exceeds a predefined threshold s_{thr}, i.e.,:

$$|s_k| > s_{thr}, \tag{4}$$

and this condition is satisfied symmetrically in both directions from the central pixel with consistent slope orientation, the lower (or higher) pixels are classified as pits (or peaks), respectively (Figure 6a).

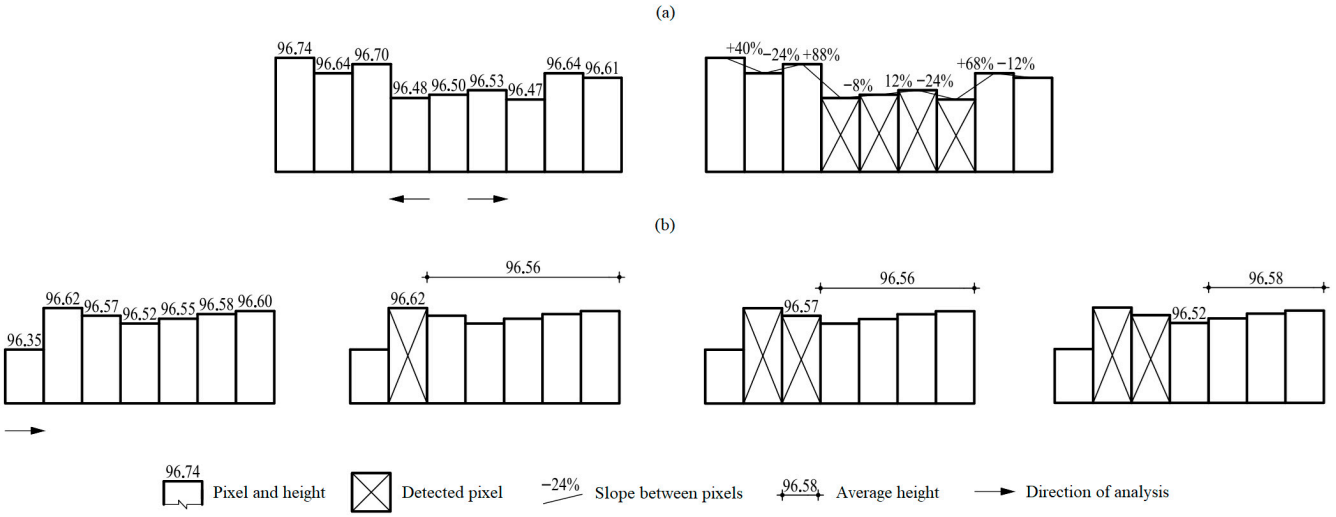

Figure 6. Illustration of the detection of pixels selected for targeted smoothing in the case of pits/peaks (**a**) and half-pits/half-peaks (**b**).

For half-pits and half-peaks, the analysis begins with the first two pixels of the vector. If the slope threshold condition (Equation (4)) is met, the algorithm proceeds along the vector by comparing each currently examined pixel, with the mean elevation in the remaining pixels ahead in the vector. The mean elevation in the remaining pixels from index $k + 1$ to n is defined as follows:

$$\overline{z}_{k+1:n} = \frac{1}{n-k} \sum_{i=k+1}^{n} z_i. \tag{5}$$

In case of half-peaks, identified by:

$$z_1 < z_2, \tag{6}$$

the detection continues as long as the following is observed:

$$\overline{z}_{k+1:n} < z_k, \tag{7}$$

holds for $k = 2, \ldots, n - 1$. For half-pits, the same criteria defined in Equations (6) and (7) apply with inverted inequality. The evaluation proceeds iteratively along the vector until the end of the vector is reached or the condition is no longer satisfied (Figure 6b).

The detected pixels form contiguous areas. Their smoothing, i.e., recalculation of elevation values, is performed using inverse distance weighting (IDW) interpolation:

$$z_p = \frac{\sum_{i=1}^{m} \frac{z_i}{d_i^k}}{\sum_{i=1}^{m} \frac{1}{d_i^k}}, \tag{8}$$

where the weighting parameter was set as $k = 2$. All neighbouring non-artifact pixels surrounding the connected region were included in the interpolation.

For detection and smoothing, pit lengths of 9 pixels and half-pit lengths of 7 pixels (corresponding to 2.25 m and 1.75 m, respectively) were used, while slope thresholds of 40% and 60% were applied. As a result, two smoothed models were generated for each parameter combination, and the corresponding unsmoothed model was also included in the analysis.

The processing steps and the branching structure of the workflow are summarised in Figure 7. Considering the initial 27 flight parameter combinations per sample area, the maximum possible number of generated DTMs was 32,400.

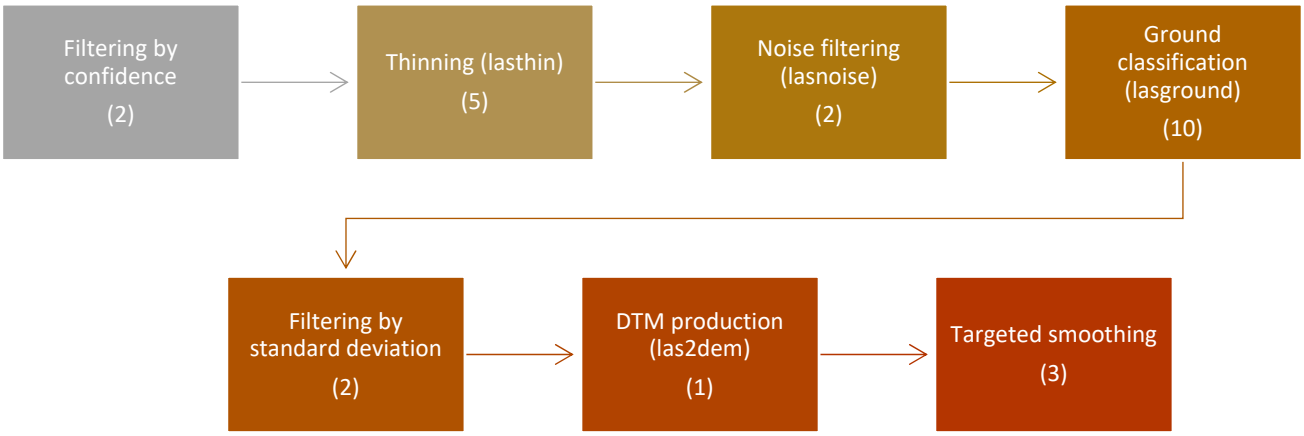

Figure 7. Workflow of DTM generation, including the number of possible parameter values at each processing step.

2.4. Accuracy Analysis

The terrain models generated for each sample area (up to 32,400 combinations) were compared to the reference models, producing difference rasters. These were subjected to statistical analysis within the boundaries of the sample areas, corresponding to approximately 160,000 values per area. The following metrics were evaluated:

- Global minimum;
- Global maximum;
- Mean of absolute values;
- 99% quantile of absolute values;
- Maximum of absolute values.

After deriving these statistical metrics, the influence of individual variables and their respective parameter values on the results was analysed.

For this purpose, SHAP (SHapley Additive exPlanations) analysis was applied in a Python (v3.13) programming environment. SHAP is a game theory–based interpretability method that assigns a value to each input variable, indicating how much it increases or decreases the model prediction relative to a baseline mean. The resulting values are signed, reflecting whether individual input parameters have a positive or negative effect on the

output. By averaging the absolute SHAP values, the global importance of each variable can be determined [59].

The analysis was conducted separately for each of the four sample areas and subsequently for the merged dataset. This approach allows for an assessment of whether the input variables influence model accuracy consistently across different areas or whether their effects vary depending on site-specific conditions.

3. Results

Image matching proved to be the most successful in Sample area 2, where stable exterior orientation was achieved under all examined flight parameter settings. This can be attributed to the uniform, diffuse illumination conditions and the sparser canopy and branch structure. In denser forest stands and areas with rough topography (Sample areas 1 and 3), the success of image matching was primarily limited by varying illumination and slope. At lower flight altitudes, reliable matching could only be ensured by increasing image overlap. In Sample area 4, despite the more favourable terrain conditions, short periods of direct illumination also reduced the performance of low-overlap configurations, although to a smaller extent than in steeper areas. Overall, considering all four sample areas, successful image matching was achieved in 79.6% of the tested parameter combinations.

The magnitude of the 3D errors of the GCPs strongly depends on flight altitude and image overlap, i.e., on the number of images. In cases with higher overlaps and thus a larger number of images, this error ranged between 2–3 cm, whereas under lower image densities it decreased to 1–2 cm. A similar trend can be observed for point density: at the highest image counts, point densities reach up to 1000 points/m^2, while at the lowest overlap settings, this value is reduced by approximately half. The application of the reliability filter reduces the point count to roughly two thirds of its original value. A comparable reduction is observed when thinning is applied using cells with a side length of 5 cm, while ground point classification results in an additional reduction of approximately 15%. The individual noise filtering procedures have only a negligible effect at this scale. Since thinning limits the theoretical maximum point density to 400 points/m^2, depending on the applied flight parameters and filtering steps, terrain models were generated from point clouds with an average density of 150–350 points/m^2 when the reliability filter was applied, and 250–380 points/m^2 when it was omitted.

By analysing the effects of various processing steps and parameter combinations applied to the generated point clouds and terrain models, it is possible to determine which elements should be included in the processing workflow and with which parameter values. During the analysis, five different statistical metrics were derived from the difference rasters. Among these, the most important indicator is the mean of the absolute deviations from the reference model, which represents the mean absolute error of the generated terrain model.

In addition to the mean absolute error, reliability can be characterized by the magnitude of outliers; therefore, the maximum positive and negative deviations were also considered as key metrics. The frequency of outliers is reflected by the extent of the quantile intervals. The statistical characteristics of the parameter combinations yielding the lowest mean absolute deviations are presented in Table 2, while their distribution is shown on Figure 8.

Table 2. Statistical indicators of the most accurate DTMs per sample area (in meters).

Stat. Values	Sample Area 1	Sample Area 2	Sample Area 3	Sample Area 4
Minimum	−0.398	−0.358	−0.411	−0.302
Maximum	0.252	0.354	0.213	0.248
Absolute mean	0.060	0.049	0.055	0.050
99% quantile	0.182	0.195	0.203	0.195
Absolute maximum	0.398	0.358	0.411	0.302

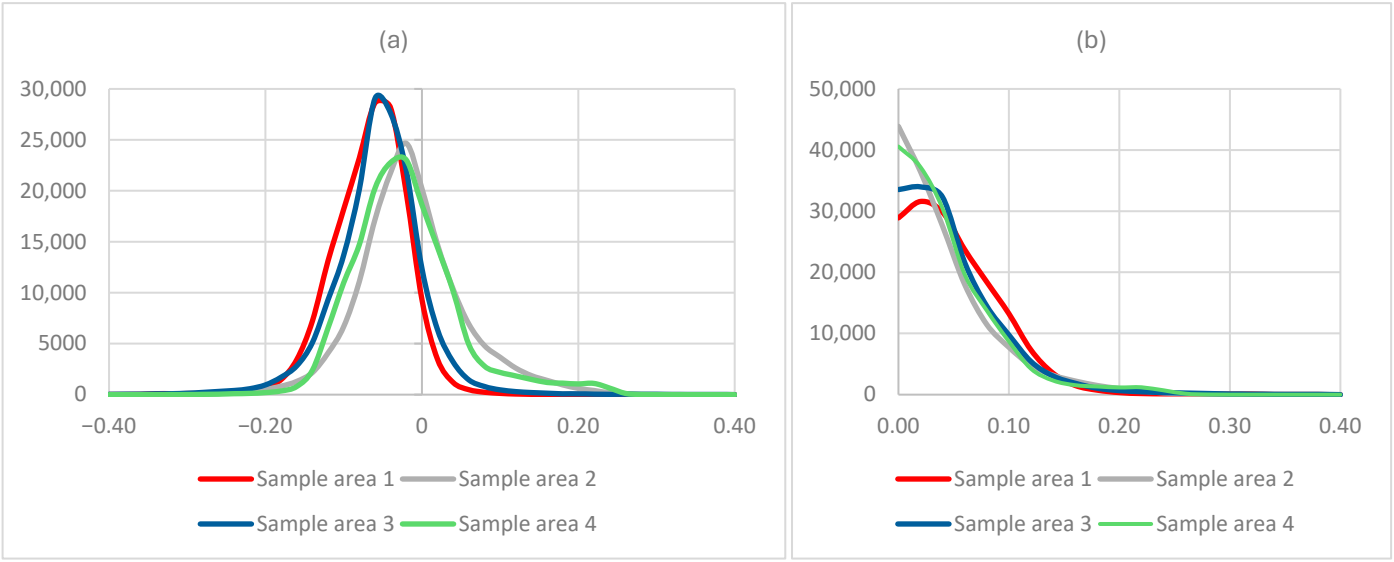

Figure 8. Distribution of deviations (**a**) and absolute deviations (**b**) by sample area.

3.1. Mean Absolute Deviation

Figure 9 presents the relative influence of the individual flight and processing parameters based on the SHAP analysis. Flight altitude, front overlap, and side overlap exhibit the strongest influence, reflecting the fundamental role of these parameters. The ground classification scale also shows a generally significant contribution. While notable variability can be observed between individual sample areas, their combined effect becomes more balanced when all areas are considered together. For this parameter, neither standard deviation–based filtering nor targeted smoothing shows substantial overall importance; the former exhibits a noticeable effect only in Sample area 4. The differences between sample areas clearly indicate that terrain conditions, forest stand structure, and illumination conditions during image acquisition require individual combination of processing steps and parameter values.

Table 3 summarizes the effects of individual flight parameters on the mean absolute deviation. Since lower deviations correspond to higher terrain model accuracy, negative values indicate better quality, i.e., a reduction in the mean deviation. Overall, a flight altitude of 100 m yields the best results, with Sample area 1 being a notable exception. This deviation is likely due to the more uniform illumination conditions during the 120 m flight, whereas data acquisition at 100 m and 80 m alternated between diffuse and direct illumination. Regarding front overlap, an overlap of 80% produced the most favourable results, contradicting the common assumption that higher overlap (and thus a larger number of images) necessarily leads to higher accuracy. This trend does not apply to side overlap, where 90% clearly outperforms the other tested values; the remaining two options result in below-average accuracy.

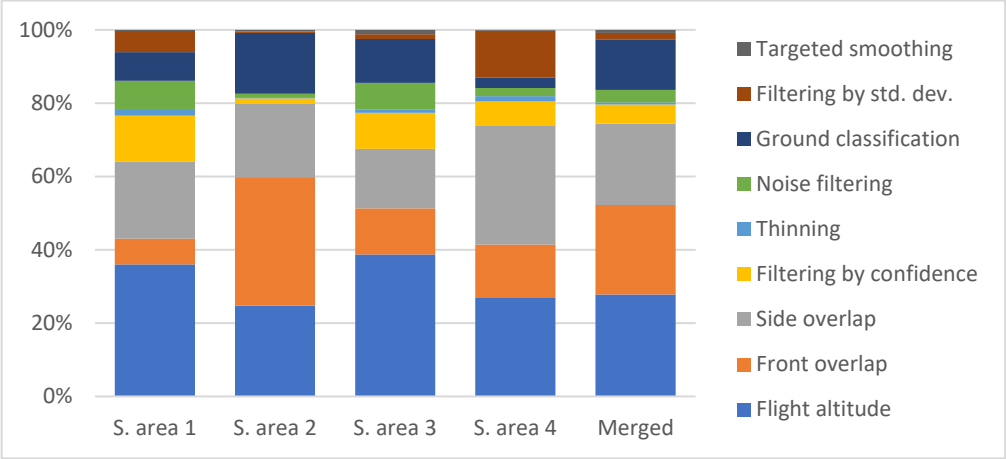

Figure 9. Relative importance according to SHAP for the mean absolute deviation.

Table 3. Effect of flight parameters on the mean absolute deviation (in meters).

Sample Area	Flight Altitude [m]			Front Overlap [%]			Side Overlap [%]		
	120	100	80	90	80	70	90	80	70
Sample area 1	−0.057	0.041	0.073	0.006	−0.014	−0.011	−0.037	0.017	0.046
Sample area 2	0.199	−0.081	−0.120	−0.152	−0.142	0.282	−0.132	−0.025	0.158
Sample area 3	0.240	−0.210	0.032	−0.012	0.029	−0.035	−0.033	0.069	0.042
Sample area 4	0.013	−0.003	−0.007	0.000	−0.003	0.007	−0.003	−0.010	0.021
Merged	0.093	−0.061	−0.050	−0.034	−0.062	0.114	−0.060	0.003	0.082

The results discussed above illustrate only the individual effects of each parameter; therefore, Table 4 presents the combination of the three flight parameters for the merged dataset. At an altitude of 120 m, slightly better-than-average results are achieved with front overlaps of 90% and 80% combined with a side overlap of 90%, as well as with the 80–70% combination. At 100 m, all combinations except 70–70% yield improved values, with 70–90% and 80–80% proving to be the most effective, albeit only marginally. Interestingly, at 80 m altitude, the configuration with the highest image count (i.e., the highest overlap combination) results in below-average accuracy, while the 80–80% combination again provides the best performance.

Table 4. Combined effects of the three flight parameters on the mean absolute deviation (in meters).

Altitude	120 m			100 m			80 m		
Front (↓)/Side (⟶) Overlap	90%	80%	70%	90%	80%	70%	90%	80%	70%
90%	−0.024	0.000	0.018	−0.031	−0.030	−0.017	0.011	−0.022	−0.004
80%	−0.017	0.058	−0.011	−0.037	−0.039	−0.035	−0.036	−0.040	−0.036
70%	0.016	0.118	0.264	−0.039	−0.020	0.127	−0.035	−0.019	0.015

In addition to the three flight parameters, the ground point classification scale also plays a substantial role in shaping the final results. Since ten different scale values were examined, their effects are illustrated using a line chart (Figure 10). In Sample areas 1 and 4, the values remain close to zero, indicating that variations in the classification scale do not significantly affect the results. In contrast, notable changes can be observed in the other two areas. In Sample area 2, increasing the scale leads to a continuous decrease in the mean absolute deviation, resulting in increasingly accurate DTMs. In Sample area 3, a similar decrease is observed initially; however, increasing the scale from 9 to 10 results in a sudden

jump, beyond which larger deviations can be expected. When all four areas are considered, a scale of 9 m yields the most favourable overall result.

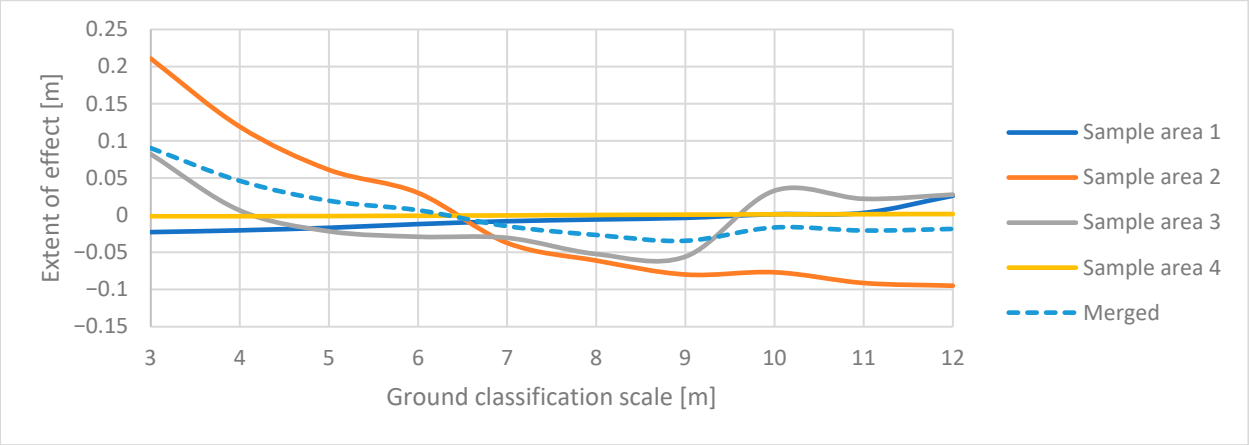

Figure 10. Effect of ground classification scale on the mean absolute deviation.

3.2. Extent of the Quantile Interval

The magnitude of outlier errors is characterized by the 99% quantile of the absolute deviations. This value indicates that the deviation of a randomly selected pixel falls below the given threshold with a probability of $p = 0.99$.

The relative impact of the individual variables shows a pattern similar to that observed for the mean absolute deviation: more than 70% of the influence originates from the flight parameters, while nearly 10% is attributable to the classification scale. Because reducing outlier errors has a more pronounced effect on this metric, the importance of targeted smoothing increases accordingly; however, its contribution remains limited to only a few percentage points, suggesting that the number of extreme outliers is relatively small.

Figure 11 illustrates the effects of individual flight and ground classification parameters on this metric. Sample area 1 and 4 clearly show similar trends across both of them, with the effects of the variables being negligible compared to those observed for the other two plots. The largest variations are observed for Sample area 2, where higher flight altitudes, greater overlaps, and larger classification scales clearly result in better performance. For Sample area 3, however, no consistent trend can be seen at the flight parameters, as a flight altitude of 100 m performs significantly better, while 80% overlaps clearly perform worse.

Considering the merged dataset, flight altitudes of 80 m and 100 m yield nearly similar results. For front overlap, 90% performs slightly better than 80%, whereas for side overlap, 90% clearly provides the best performance. Regarding the classification scale, the results are more consistent: on average, a continuous improvement is observed, although beyond 9 m the gains become negligible.

3.3. Minimum, Maximum, and Absolute Deviations

Considering the merged dataset, flight parameters and classification scale remain influential for extreme deviations; however, reliability filtering and noise filtering exhibit a more pronounced effect compared to the previously discussed metrics (Figure 12). Since both are designed to suppress point cloud noise, this behaviour is expected. Nevertheless, targeted smoothing has an even greater impact on the final results, as it operates not on the point cloud but directly on the derived raster, effectively applying a secondary noise-reduction process.

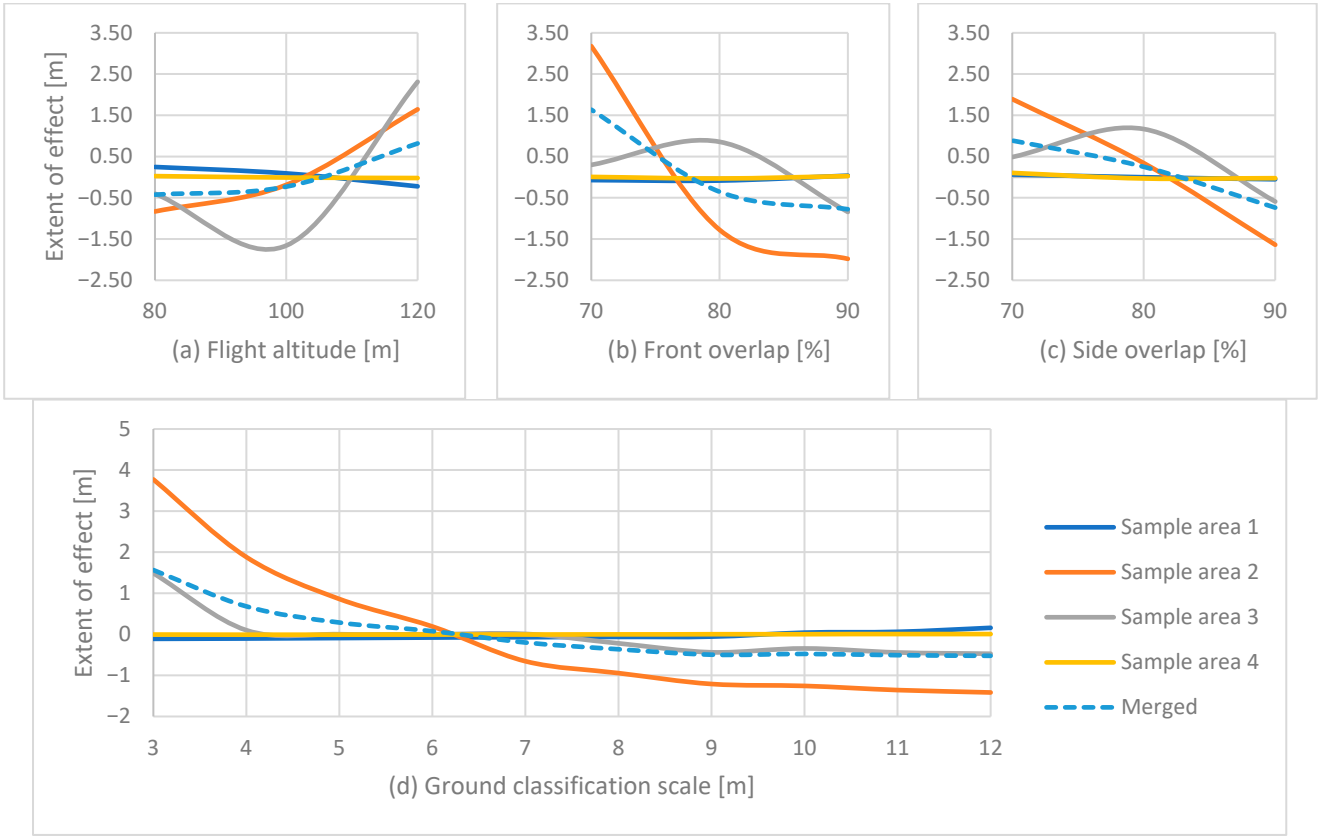

Figure 11. Effect of flight altitude (**a**), front overlap (**b**), side overlap (**c**), and ground classification scale (**d**) on the 99% quantile of the deviations.

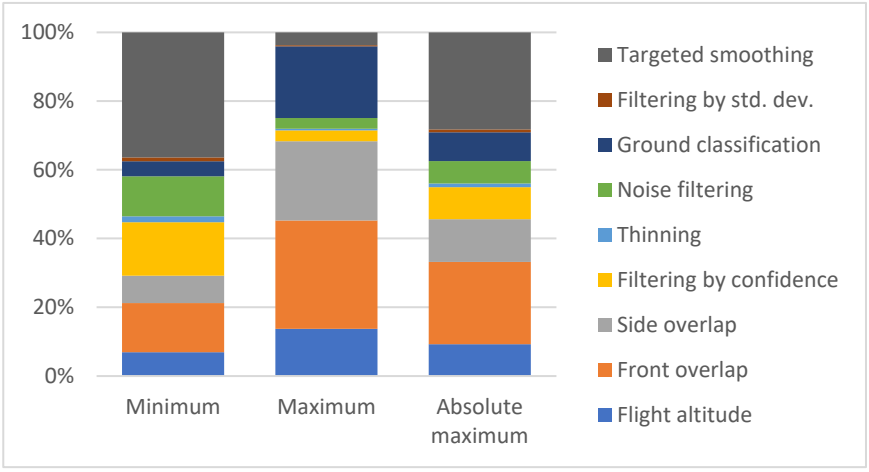

Figure 12. Relative impact according to SHAP for minimum and maximum deviations and their absolute values.

For minimum deviations, a substantial effect exceeding one meter can be observed, indicating that the method effectively removes below-ground point cloud noise that remains after other filtering approaches, now applied in raster form. The application of the method also reduces the maximum deviations. For the maximum of the absolute deviations, the effect magnitude is largely governed by the absolute values of the minima. A smaller difference can also be observed between the two tested slope thresholds, with the 40% threshold generally producing better results (Table 5).

Table 5. Effect of targeted smoothing on minimum and maximum deviations and their absolute values.

Metric	Smoothing Excluded	Slope Limit [%]	
		40	60
Minimum	−3.153	1.607	1.529
Maximum	0.226	−0.117	−0.080
Absolute maximum	2.996	−1.562	−1.466

4. Discussion

The most fundamental metric for assessing terrain model accuracy is the mean deviation from a reference surface, expressed in absolute terms. Among the flight parameters, the importance of flight altitude increases under variable illumination conditions and in areas with dense branch structures, while improved ground visibility somewhat reduces its influence; nevertheless, this parameter remains highly significant overall. Front overlap plays a particularly important role in areas with steeper slopes that include not only deciduous stands but also larger coniferous patches. In contrast, side overlap appears to be more influential in areas with less rough terrain.

The fact that, considering the merged dataset, a front overlap of 80% performs better than 90% is quite unexpected regarding several studies that have shown that higher overlaps, above a certain level, generally result in improved accuracy, albeit not always substantially [11,16,60]. However, it is not unprecedented that in certain cases, extremely high overlaps can produce the opposite effect [61]. When examined individually, this trend is particularly noticeable in Sample areas 1 and 4. This is likely attributable to the relatively sparse canopy structure in these stands, which allows the ground surface to be reconstructed almost perfectly even at lower overlaps, while higher, 90% front overlaps may introduce unexpected geometric errors due to the short baseline between images, especially over homogeneous ground cover. In areas where the canopy structure is denser and larger coniferous patches are present (Sample areas 2 and 3), this trend is no longer observed. Regarding flight altitude, the better performance at 100 m and 80 m contrasts with the 120 m considered optimal by Dhruva et al. [13].

For the 99% quantile of deviations, which reflects model reliability, front overlap shows clear dominance among the three flight parameters. The effects of different stand characteristics are also clearly distinguishable. The similar, relatively low-magnitude trend observed in Sample areas 1 and 4, compared to the other two areas, can be attributed to the sparser canopy structure, which allows none of the flight parameters to significantly influence the near-perfect coverage of ground points across the area; so, there was no need to rely on interpolation over larger contiguous areas.

Among the point cloud processing steps, both the mean absolute deviation and the 99% quantile of deviations are primarily influenced by the ground point classification scale. This effect is particularly pronounced in forest stands with dense canopy structures and extensive coniferous patches, where ground points are more sparsely distributed. In contrast, in areas with a more uniform ground point distribution, the influence of this parameter is considerably weaker, as well as at the flight parameters.

Based on the results, contrast variations caused by changing illumination conditions do not significantly affect the classification scale. Quantitatively, a classification scale of 9 m is recommended for forested areas when using the lasground module of LAStools. This parameter also exerts the strongest influence on the 99% quantile of deviations, while the effects of other processing parameters are generally negligible.

Regarding the outlier errors, minimum deviations are most strongly affected by targeted smoothing, whereas maximum deviations are primarily influenced by the classification scale. When considering absolute extreme values, targeted smoothing remains the dominant factor. The targeted smoothing method developed in this study can remove surface artifacts originating from noise points that are not eliminated by conventional filtering approaches. As a result, it substantially reduces the magnitude of the largest outliers, effectively mitigating gross errors in the generated models.

5. Conclusions

Based on the numerical results, higher flight altitudes require larger overlaps, whereas at lower altitudes, it is advisable to reduce overlap values—until image matching success is not compromised. This is likely attributable to the reduced number of images, which in turn results in lower noise levels. According to the above findings, the following processing steps and parameter values are recommended for producing terrain models in forested areas with appropriate accuracy:

- Flight altitude: 100 m;
- Front overlap: 80%;
- Side overlap: 90%;
- Reliability filter: removal of low-confidence points (confidence value = 1);
- Thinning: retention of the lowest point within cells of 5 cm side length;
- Ground classification (lasground) scale: 9 m;
- Targeted smoothing: slope threshold of 40%.

The resulting DTMs exhibit a mean error of approximately 6 cm and a maximum outlier error of about 40 cm. Although these accuracies may not appear particularly high from a geodetic perspective, in forestry applications—where such models are primarily used for tree height estimation, for which a vertical resolution of approximately 0.1 m is generally sufficient—they clearly qualify for the normalization of canopy height models. Nevertheless, flights conducted under stable, diffuse illumination conditions are still strongly recommended, as varying light not only reduces image matching success but also significantly increases noise levels, which cannot always be fully eliminated by filtering procedures.

Overall, the results demonstrate that UAV-based photogrammetry, when combined with appropriately selected flight and processing parameters, is capable of producing terrain models of sufficient accuracy even in forested environments. The analyses clearly confirm that careful parameter tuning, and targeted, terrain-specific noise filtering jointly play a key role in improving accuracy and reducing extreme errors, thereby providing a reliable foundation for subsequent forestry applications.

Author Contributions: Conceptualization, B.S.; methodology, B.S.; software, B.S., G.B. and G.K.; validation, B.S.; formal analysis, B.S.; investigation, B.S.; resources, B.S., G.B. and G.K.; data curation, B.S.; writing—original draft preparation, B.S.; writing—review and editing, G.B. and G.K.; visualization, B.S.; supervision, G.K.; project administration, G.B.; funding acquisition, G.B. All authors have read and agreed to the published version of the manuscript.

Funding: This article was devised in the framework of the project TKP2021-NVA-13, which has been implemented with the support provided by the Ministry of Culture and Innovation of Hungary from the National Research, Development and Innovation Fund, financed under the TKP2021-NVA funding scheme.

Data Availability Statement: The data that support the findings of this study are available from the corresponding author upon reasonable request.

Acknowledgments: We would like to thank the colleagues of the Institute of Geomatics and Civil Engineering, and the students of the Faculty of Forestry for their help with the field reference measurements. We also thank the CEOs of the involved forestry companies for their permission to conduct this research on their territory.

Conflicts of Interest: The authors declare no conflicts of interest.

Abbreviations

The following abbreviations are used in this manuscript:

UAV	Unmanned Aerial Vehicle
DTM	Digital Terrain Model
GCP	Ground Control Point
TLS	Terrestrial Laser Scanning
SfM	Structure-from-Motion
SHAP	SHapley Additive exPlanations

References

1. Krause, S.; Sanders, T.G.M.; Mund, J.-P.; Greve, K. UAV-Based Photogrammetric Tree Height Measurement for Intensive Forest Monitoring. *Remote Sens.* **2019**, *11*, 758. [CrossRef]
2. Vacca, G.; Vecchi, E. UAV Photogrammetric Surveys for Tree Height Estimation. *Drones* **2024**, *8*, 106. [CrossRef]
3. Szász, B.; Heil, B.; Kovács, G.; Mészáros, D.; Czimber, K. Comparison of Advanced Terrestrial and Aerial Remote Sensing Methods for Above-Ground Carbon Stock Estimation—A Comparative Case Study for a Hungarian Temperate Forest. *Remote Sens.* **2025**, *17*, 2173. [CrossRef]
4. Kameyama, S.; Sugiura, K. Estimating Tree Height and Volume Using Unmanned Aerial Vehicle Photography and SfM Technology, with Verification of Result Accuracy. *Drones* **2020**, *4*, 19. [CrossRef]
5. Kachamba, D.J.; Ørka, H.O.; Gobakken, T.; Eid, T.; Mwase, W. Biomass Estimation Using 3D Data from Unmanned Aerial Vehicle Imagery in a Tropical Woodland. *Remote Sens.* **2016**, *8*, 968. [CrossRef]
6. Maesano, M.; Santopuoli, G.; Moresi, F.V.; Matteucci, G.; Lasserre, B.; Scarascia Mugnozza, G. Above Ground Biomass Estimation from UAV High Resolution RGB Images and LiDAR Data in a Pine Forest in Southern Italy. *iForest—Biogeosci. For.* **2022**, *15*, 451. [CrossRef]
7. Jia, X.; Wang, C.; Da, Y.; Tian, X.; Ge, W. Tree-Level Biomass Estimation Using Unmanned Aerial Vehicle (UAV) Imagery and Allometric Equation. *Biomass Bioenergy* **2024**, *190*, 107420. [CrossRef]
8. Juan-Ovejero, R.; Elghouat, A.; Navarro, C.J.; Reyes-Martín, M.P.; Jiménez, M.N.; Navarro, F.B.; Alcaraz-Segura, D.; Castro, J. Estimation of Aboveground Biomass and Carbon Stocks of *Quercus Ilex* L. Saplings Using UAV-Derived RGB Imagery. *Ann. For. Sci.* **2023**, *80*, 44. [CrossRef]
9. Czimber, K.; Szász, B.; Ács, N.; Heilig, D.; Illés, G.; Mészáros, D.; Veperdi, G.; Heil, B.; Kovács, G. Estimation of the Total Carbon Stock of Dudles Forest Based on Satellite Imagery, Airborne Laser Scanning, and Field Surveys. *Forests* **2025**, *16*, 512. [CrossRef]
10. Szász, B.; Heil, B.; Kovács, G.; Heilig, D.; Veperdi, G.; Mészáros, D.; Illés, G.; Czimber, K. Investigation of the Relationship between Topographic and Forest Stand Characteristics Using Aerial Laser Scanning and Field Survey Data. *Forests* **2024**, *15*, 1546. [CrossRef]
11. Pessacg, F.; Gómez-Fernández, F.; Nitsche, M.; Chamo, N.; Torrella, S.; Ginzburg, R.; Cristóforis, P.D. Simplifying UAV-Based Photogrammetry in Forestry: How to Generate Accurate Digital Terrain Model and Assess Flight Mission Settings. *Forests* **2022**, *13*, 173. [CrossRef]
12. Nex, F.; Remondino, F. UAV for 3D Mapping Applications: A Review. *Appl. Geomat.* **2014**, *6*, 1–15. [CrossRef]
13. Dhruva, A.; Hartley, R.J.L.; Redpath, T.A.N.; Estarija, H.J.C.; Cajes, D.; Massam, P.D. Effective UAV Photogrammetry for Forest Management: New Insights on Side Overlap and Flight Parameters. *Forests* **2024**, *15*, 2135. [CrossRef]
14. Nikolakopoulos, K.G.; Kyriou, A.; Koukouvelas, I.K. Developing a Guideline of Unmanned Aerial Vehicle's Acquisition Geometry for Landslide Mapping and Monitoring. *Appl. Sci.* **2022**, *12*, 4598. [CrossRef]
15. Kyriou, A.; Nikolakopoulos, K.; Koukouvelas, I. How Image Acquisition Geometry of UAV Campaigns Affects the Derived Products and Their Accuracy in Areas with Complex Geomorphology. *ISPRS Int. J. Geo-Inf.* **2021**, *10*, 408. [CrossRef]
16. Sadeq, H.A. Accuracy Assessment Using Different UAV Image Overlaps. *J. Unmanned Veh. Sys.* **2019**, *7*, 175–193. [CrossRef]
17. Ahmed, S.; El-Shazly, A.; Abed, F.; Ahmed, W. The Influence of Flight Direction and Camera Orientation on the Quality Products of UAV-Based SfM-Photogrammetry. *Appl. Sci.* **2022**, *12*, 10492. [CrossRef]

18. Vacca, G.; Dessì, A.; Sacco, A. The Use of Nadir and Oblique UAV Images for Building Knowledge. *ISPRS Int. J. Geo-Inf.* **2017**, *6*, 393. [CrossRef]
19. Lingua, A.; Noardo, F.; Spanò, A.; Sanna, S.; Matrone, F. 3D model generation using oblique images acquired by UAV. *ISPRS Ann. Photogramm. Remote Sens. Spat. Inf. Sci.* **2017**, *42*, 107–115. [CrossRef]
20. Hugenholtz, C.; Brown, O.; Walker, J.; Barchyn, T.E.; Nesbit, P.; Kucharczyk, M.; Myshak, S. Spatial Accuracy of UAV-Derived Orthoimagery and Topography: Comparing Photogrammetric Models Processed with Direct Geo-Referencing and Ground Control Points. *Geomatica* **2016**, *70*, 21–30. [CrossRef]
21. Štroner, M.; Urban, R.; Reindl, T.; Seidl, J.; Brouček, J. Evaluation of the Georeferencing Accuracy of a Photogrammetric Model Using a Quadrocopter with Onboard GNSS RTK. *Sensors* **2020**, *20*, 2318. [CrossRef]
22. Tahar, K.N. An Evaluation on Different Number of Ground Control Points in Unmanned Aerial Vehicle Photogrammetric Block. *Int. Arch. Photogramm. Remote Sens. Spat. Inf. Sci.* **2013**, *XL-2/W2*, 93–98. [CrossRef]
23. Sanz-Ablanedo, E.; Chandler, J.H.; Rodríguez-Pérez, J.R.; Ordóñez, C. Accuracy of Unmanned Aerial Vehicle (UAV) and SfM Photogrammetry Survey as a Function of the Number and Location of Ground Control Points Used. *Remote Sens.* **2018**, *10*, 1606. [CrossRef]
24. Verykokou, S.; Ioannidis, C. Image Matching: A Comprehensive Overview of Conventional and Learning-Based Methods. *Encyclopedia* **2025**, *5*, 4. [CrossRef]
25. Karami, E.; Prasad, S.; Shehata, M. Image Matching Using SIFT, SURF, BRIEF and ORB: Performance Comparison for Distorted Images. *arXiv* **2017**. [CrossRef]
26. Hirschmuller, H. Accurate and Efficient Stereo Processing by Semi-Global Matching and Mutual Information. In Proceedings of the 2005 IEEE Computer Society Conference on Computer Vision and Pattern Recognition (CVPR'05), San Diego, CA, USA, 20–25 June 2005; Volume 2, pp. 807–814. Available online: https://ieeexplore.ieee.org/document/1467526 (accessed on 25 December 2025).
27. Furukawa, Y.; Hernández, C. Multi-View Stereo: A Tutorial. *Found. Trends Comput. Graph. Vis.* **2015**, *9*, 1–148. [CrossRef]
28. Westoby, M.J.; Brasington, J.; Glasser, N.F.; Hambrey, M.J.; Reynolds, J.M. 'Structure-from-Motion' Photogrammetry: A Low-Cost, Effective Tool for Geoscience Applications. *Geomorphology* **2012**, *179*, 300–314. [CrossRef]
29. Iglhaut, J.; Cabo, C.; Puliti, S.; Piermattei, L.; O'Connor, J.; Rosette, J. Structure from Motion Photogrammetry in Forestry: A Review. *Curr. For. Rep.* **2019**, *5*, 155–168. [CrossRef]
30. Verhoeven, G.; Doneus, M.; Briese, C.; Vermeulen, F. Mapping by Matching: A Computer Vision-Based Approach to Fast and Accurate Georeferencing of Archaeological Aerial Photographs. *J. Archaeol. Sci.* **2012**, *39*, 2060–2070. [CrossRef]
31. Harwin, S.; Lucieer, A.; Osborn, J. The Impact of the Calibration Method on the Accuracy of Point Clouds Derived Using Unmanned Aerial Vehicle Multi-View Stereopsis. *Remote Sens.* **2015**, *7*, 11933–11953. [CrossRef]
32. Polat, N.; Uysal, M. An Experimental Analysis of Digital Elevation Models Generated with Lidar Data and UAV Photogrammetry. *J. Indian Soc. Remote Sens.* **2018**, *46*, 1135–1142. [CrossRef]
33. Xiong, B.; Oude Elberink, S.; Vosselman, G. Building Modeling from Noisy Photogrammetric Point Clouds. *ISPRS Ann. Photogramm. Remote Sens. Spat. Inf. Sci.* **2014**, *II–3*, 197–204. [CrossRef]
34. Ren, Y.; Li, T.; Xu, J.; Hong, W.; Zheng, Y.; Fu, B. Overall Filtering Algorithm for Multiscale Noise Removal From Point Cloud Data. *IEEE Access* **2021**, *9*, 110723–110734. [CrossRef]
35. Wang, M.; Zheng, F.; Wang, Y.; Sun, Z. Time-of-Flight Point Cloud Denoising Method Based on Confidence Level. *Infrared Technol.* **2022**, *44*, 513–520. Available online: http://hwjs.nvir.cn/en/article/id/514bff62-77ef-48f3-8b8d-439162f6510f (accessed on 10 December 2025).
36. Salehi, B.; Jarahizadeh, S.; Sarafraz, A. An Improved RANSAC Outlier Rejection Method for UAV-Derived Point Cloud. *Remote Sens.* **2022**, *14*, 4917. [CrossRef]
37. Liu, X. Airborne LiDAR for DEM Generation: Some Critical Issues. *Prog. Phys. Geogr. Earth Environ.* **2008**, *32*, 31–49. [CrossRef]
38. Sithole, G.; Vosselman, G. Experimental Comparison of Filter Algorithms for Bare-Earth Extraction from Airborne Laser Scanning Point Clouds. *ISPRS J. Photogramm. Remote Sens.* **2004**, *59*, 85–101. [CrossRef]
39. Sithole, G. Filtering of Laser Altimetry Data Using a Slope Adaptive Filter. *Int. Arch. Photogramm. Remote Sens.* **2001**, *34*, 203–210. Available online: https://www.isprs.org/proceedings/xxxiv/3-w4/pdf/sithole.pdf (accessed on 12 December 2025).
40. Vosselman, G. Slope Based Filtering of Laser Altimetry Data. *Int. Arch. Photogramm. Remote Sens.* **2000**, *33*, 958–964.
41. Murphy, P.N.C.; Ogilvie, J.; Meng, F.-R.; Arp, P. Stream network modelling using lidar and photogrammetric digital elevation models: A comparison and field verification. *Hydrol. Process.* **2008**, *22*, 1747–1754. [CrossRef]
42. Glenn, N.F.; Spaete, L.P.; Sankey, T.T.; Derryberry, D.R.; Hardegree, S.P.; Mitchell, J.J. Errors in LiDAR-Derived Shrub Height and Crown Area on Sloped Terrain. *J. Arid Environ.* **2011**, *75*, 377–382. [CrossRef]
43. Kraus, K.; Pfeifer, N. Determination of Terrain Models in Wooded Areas with Airborne Laser Scanner Data. *ISPRS J. Photogramm. Remote Sens.* **1998**, *53*, 193–203. [CrossRef]

44. Hu, H.; Ding, Y.; Zhu, Q.; Wu, B.; Lin, H.; Du, Z.; Zhang, Y.; Zhang, Y. An Adaptive Surface Filter for Airborne Laser Scanning Point Clouds by Means of Regularization and Bending Energy. *ISPRS J. Photogramm. Remote Sens.* **2014**, *92*, 98–111. [CrossRef]
45. Lohmann, P. Segmentation and Filtering of Laser Scanner Digital Surface Models. *Int. Arch. Photogramm. Remote Sens. Spat. Inf. Sci.* **2002**, *34*, 311–316.
46. Yan, M.; Blaschke, T.; Liu, Y.; Wu, L. An Object-Based Analysis Filtering Algorithm for Airborne Laser Scanning. *Int. J. Remote Sens.* **2012**, *33*, 7099–7116. [CrossRef]
47. Meng, X.; Currit, N.; Zhao, K. Ground Filtering Algorithms for Airborne LiDAR Data: A Review of Critical Issues. *Remote Sens.* **2010**, *2*, 833–860. [CrossRef]
48. Klápště, P.; Fogl, M.; Barták, V.; Gdulová, K.; Urban, R.; Moudrý, V. Sensitivity Analysis of Parameters and Contrasting Performance of Ground Filtering Algorithms with UAV Photogrammetry-Based and LiDAR Point Clouds. *Int. J. Digit. Earth* **2020**, *13*, 1672–1694. [CrossRef]
49. Kraus, K.; Pfeifer, N. A New Method for Surface Reconstruction from Laser Scanner Data. *Int. Arch. Photogramm. Remote Sens.* **1997**, *32*, 80–86.
50. Axelsson, P. DEM Generation from Laser Scanner Data Using Adaptive TIN Models. *Int. Arch. Photogramm. Remote Sens.* **2000**, *33*, 110–117. Available online: https://cir.nii.ac.jp/crid/1573950400217278336 (accessed on 12 December 2025).
51. Dong, Y.; Cui, X.; Zhang, L.; Ai, H. An Improved Progressive TIN Densification Filtering Method Considering the Density and Standard Variance of Point Clouds. *ISPRS Int. J. Geo-Inf.* **2018**, *7*, 409. [CrossRef]
52. Pingel, T.J.; Clarke, K.C.; McBride, W.A. An Improved Simple Morphological Filter for the Terrain Classification of Airborne LIDAR Data. *ISPRS J. Photogramm. Remote Sens.* **2013**, *77*, 21–30. [CrossRef]
53. Zhang, K.; Chen, S.-C.; Whitman, D.; Shyu, M.-L.; Yan, J.; Zhang, C. A Progressive Morphological Filter for Removing Nonground Measurements from Airborne LIDAR Data. *IEEE Trans. Geosci. Remote Sens.* **2003**, *41*, 872–882. [CrossRef]
54. Zhang, W.; Qi, J.; Wan, P.; Wang, H.; Xie, D.; Wang, X.; Yan, G. An Easy-to-Use Airborne LiDAR Data Filtering Method Based on Cloth Simulation. *Remote Sens.* **2016**, *8*, 501. [CrossRef]
55. Li, F.; Zhu, H.; Luo, Z.; Shen, H.; Li, L. An Adaptive Surface Interpolation Filter Using Cloth Simulation and Relief Amplitude for Airborne Laser Scanning Data. *Remote Sens.* **2021**, *13*, 2938. [CrossRef]
56. Cai, S.; Zhang, W.; Liang, X.; Wan, P.; Qi, J.; Yu, S.; Yan, G.; Shao, J. Filtering Airborne LiDAR Data Through Complementary Cloth Simulation and Progressive TIN Densification Filters. *Remote Sens.* **2019**, *11*, 1037. [CrossRef]
57. Farr, T.G.; Rosen, P.A.; Caro, E.; Crippen, R.; Duren, R.; Hensley, S.; Kobrick, M.; Paller, M.; Rodriguez, E.; Roth, L.; et al. The Shuttle Radar Topography Mission. *Rev. Geophys.* **2007**, *45*. [CrossRef]
58. Anders, N.; Valente, J.; Masselink, R.; Keesstra, S. Comparing Filtering Techniques for Removing Vegetation from UAV-Based Photogrammetric Point Clouds. *Drones* **2019**, *3*, 61. [CrossRef]
59. Lundberg, S.; Lee, S.-I. A Unified Approach to Interpreting Model Predictions. *arXiv* **2017**, arXiv:1705.07874. [CrossRef]
60. Elhadary, A.; Rabah, M.; Ghanim, E.; Mohie, R.; Taha, A. The influence of flight height and overlap on UAV imagery over featureless surfaces and constructing formulas predicting the geometrical accuracy. *NRIAG J. Astron. Geophys.* **2022**, *11*, 210–223. [CrossRef]
61. Nesbit, P.R.; Hugenholtz, C.H. Enhancing UAV–SfM 3D Model Accuracy in High-Relief Landscapes by Incorporating Oblique Images. *Remote Sens.* **2019**, *11*, 239. [CrossRef]